Facilitating Basal Slip to Increase Deformation Ability in Mg-Mn-Ce Alloy by Textural Reconstruction Using Friction Stir Processing

FENG-CHAO LIU, ZONG-YI MA, and MING-JEN TAN

The widespread application of wrought magnesium alloys is hampered by their insufficient formability at room temperature. The tensile ductility of a newly developed Mg-Mn-Ce alloy has been dramatically improved by friction stir processing (FSP). The microstructure of the stir zone was characterized mainly by elongated fine grains which were highly separated by low-angle grain boundaries because of the high contribution of continuous dynamic recrystallization. A new {0002} distribution with high basal plane tilt angles which facilitated ⟨a⟩ basal slip when the specimens were pulled along the FSP direction was obtained. Both the enhanced basal slip and crystallographic orientation evolution of Mg crystals increased the strain hardening exponent of the FSP specimen, and hence improved its tensile ductility. A material flow model, developed based on the local textural evolution, could reasonably explain the phenomenon that the FSP specimen exhibited warping and a high normal anisotropy ratio during tensile test.

DOI: 10.1007/s11661-013-1746-3

I. INTRODUCTION

OWING to the importance of fuel economy and environmental awareness, magnesium alloys have been increasingly adopted in automotive and aerospace industries and are expected to be extensively used in the future, because of their low density, high strength/mass ratio, and good recycling efficiency.[1,2] Wrought Mg alloys attract special attention since they have better mechanical properties than cast Mg alloys. However, the application of wrought Mg alloys has been strongly limited because of their poor formability at room temperature.

The poor formability of wrought Mg alloys has been attributed to the limited number of active slip systems in hexagonal close-packed (hcp) structures and to the strong basal texture generated by rolling or extrusion.[3,4] Recently, however, there have been some instances[5–8] where the ductility is improved in Mg alloys through grain refinement and/or textural development even at room temperature. A typical example is that of equal-channel angular pressing-processed AZ31B Mg alloy, with specific orientations exhibiting tremendous ductility of 45 pct combined with a low yield stress and good hardening response.[8] This suggests that the poor ductility of Mg alloys is not their intrinsic nature but relates to their microstructural conditions.

In Mg, the critical resolved shear stress (CRSS) for nonbasal slip is about one hundred times as large as that for basal slip.[9,10] The $\{10\bar{1}2\}\langle 10\bar{1}1\rangle$ twin only occurs when resolved stress is applied along the c-axis.[11] In normally rolled Mg alloys, the basal planes are oriented parallel to the rolling direction, that is, the so-called basal texture is formed.[12,13] Furthermore, the basal planes in extruded Mg alloys are oriented parallel to the extrusion direction.[14] If the rolled or extruded Mg alloys are deformed along the working direction, then the ductility is expected to be small because the shear force does not operate on the basal plane because of small Schmid factors close to 0.[15] Therefore, their workability will also be small when secondary working is carried out at room temperature using the rolled or extruded Mg alloys.

Friction stir processing (FSP) which was developed from friction stir welding (FSW)[16] has been demonstrated to be a simple, effective and versatile metal-working technique for microstructural modification.[17,18] Previous investigations[19,20] have demonstrated the effectiveness of FSP on significant breakup and dissolution of the coarse, network-like eutectic phase and on remarkable grain refinement, leading to significant enhancement in both the tensile strength and elongation-to-failure of the cast Mg alloys. A few primary studies have shown ductility improvements in the cold rolled and extruded AZ31 Mg alloys because of the textural changes during FSP.[21–23] However, a systematical study about the microstructural evolution and deformation mechanism during subsequent tensile deformation in the stir zone (SZ), especially the effect of as-received FSP microstructure on the tensile deformation behavior is still lacking.

FENG-CHAO LIU, Research Fellow, formerly with the School of Mechanical and Aerospace Engineering, Nanyang Technological University, Singapore 639798, Singapore, is now with Joining and Welding Reasearch Institute, Osaka University, Ibaraki 567-0047, Osaka, Japan. ZONG-YI MA, Full Professor, is with the Shenyang National Laboratory for Materials Science, Institute of Metal Research, Chinese Academy of Sciences, 72 Wenhua Road, Shenyang 110016, P.R. China. MING-JEN TAN, Associate Professor, is with the School of Mechanical and Aerospace Engineering, Nanyang Technological University. Contact e-mail: mmjtan@ntu.edu.sg

Manuscript submitted January 15, 2013.
Article published online April 23, 2013

MnE21 is a recently developed Mg-Mn-Ce alloy and is characterized by high corrosion resistance, sound weldability, considerable temperature resistance and low cost, which has the potential to be widely used in the automobile industry.[24] In the current study, hot-rolled MnE21 alloy was first subjected to FSP. The objectives are to: (a) investigate the material flow pattern and recrystallization mechanisms during FSP; (b) show the efficiency of using FSP to reconstruct texture and improve the formation ability of Mg alloys; and (c) clarify the textural evolution and deformation mechanism during subsequent tensile deformation and its effect on the tensile deformation behavior of Mg alloys.

II. EXPERIMENTAL

The chemical composition of MnE21 plates is listed in Table I. The as-received 5-mm-thick hot-rolled MnE21 plates with a length of 240 mm and a width of 80 mm were friction stir processed along the rolling direction using a steel tool with a concave shoulder 16 mm in diameter and a threaded conical pin 5 mm in root diameter, 4 mm in tip diameter and 3.8 mm in length. An anticlockwise rotation rate of 400 rpm and a traverse speed of 50 mm min^{-1} were selected. The tool was titled 2.5 deg away from the vertical axis opposite to the processing direction.

Tensile specimens with a gage length of 20 mm, a width of 4 mm and a thickness of 2 mm were cut from the SZ along the FSP direction (Figure 1). For comparison, same sized tensile specimens with the tensile direction parallel to the rolling and transverse directions were cut from the hot-rolled plates, respectively (hereafter denoted as RD specimen and TD specimen). Tensile tests were conducted on an Instron 8502 tester at a strain rate of 1×10^{-3} s^{-1}. At least six specimens were tested for each condition. The changes in width and thickness were measured on the failed tensile specimens around the uniformly deformed gauge region. Normal anisotropy ratio (r) were calculated in each specimen as

$$r = \Phi_w/\Phi_t \quad [1]$$

where Φ_w and Φ_t are the true plastic strains along the specimen's width w and thickness t, respectively. For the FSP specimen, Φ_w and Φ_t are estimated, respectively, by

$$\Phi_w = 1/4(\Phi_{wt} + 2\Phi_{wm} + \Phi_{wb}) \quad [2]$$

$$\Phi_t = 1/4(\Phi_{tr} + 2\Phi_{tm} + \Phi_{tl}) \quad [3]$$

where Φ_{wt}, Φ_{wm}, and Φ_{wb} are the true plastic strains along the specimen's width on the top, middle, and bottom parts, respectively; Φ_{tr}, Φ_{tm}, and Φ_{tr} are the true plastic strains along the specimen's thickness on the right, middle, and left parts, respectively.

Microstructural characterization and analysis were carried out by X-ray diffraction (XRD) and scanning electron microscopy (SEM). The specimens which were cut from the grip and gage regions of the deformed tensile specimens were lightly electropolished and then subjected to EBSD examination. EBSD orientation maps were obtained using a JSM-7600F operated at 20 kV and interfaced to an HKL Channel EBSD system. Kikuchi patterns were obtained automatically in steps of 0.33 μm. The average grain sizes of the specimens were determined by the mean linear intercept technique (grain size = 1.78 × mean linear intercept).

III. RESULTS

A. *Initial Microstructure of Hot-Rolled and FSP Specimens*

Figure 2(a) shows the EBSD map of the hot-rolled MnE21 (hereafter referred to as HR specimen). The colors in the microstructures indicate the different crystallographic orientations of the grains which can be seen in the inverse pole figures (standard orientation triangles) as shown in Figure 2(a). The black and white lines represent the high angle grain boundaries (HAGBs, grain boundary misorientation angle ≥15 deg) and low angle grain boundaries (LAGBs, grain boundary misorientation angle <15 deg), respectively. The HR specimen was characterized by equiaxed grains with an average grain size of ~21 μm. Figure 2(b) shows the frequency distribution of boundary misorientation angles for the HR specimen. The average misorientation angle was determined to be 39.3 deg. The fraction of the HAGBs was 86 pct. The textures of the HR specimens in the form of the {0002} and $\{10\bar{1}0\}$ pole figures are also illustrated in Figure 2(b). The HR specimens tended to exhibit a "basal" texture in which the majority of grains are oriented such that their {0002} basal planes are close to the plane of the sheet. However, the peak intensity is ~28 deg tilted away from the sheet normal direction (ND) toward the RD. This anisotropy may be associated with the increased activity of nonbasal slip, $\langle c+a \rangle$, at elevated temperatures.[25] The corresponding prismatic planes $\{10\bar{1}0\}$ therefore tended to orientate perpendicular to the sheet plane without distinctive preferred orientation of the $\langle 10\bar{1}0 \rangle$ poles within the basal planes.

Figure 2(c) shows the grain structure on the cross section of the FSP specimen. The location is ~2 mm away from the FSP surface. This location was selected to enable comparison with previous reports. The average grain size of the FSP specimen was ~9 μm which is significantly smaller than that of the HR specimen. Most

Table I. Nominal Composition (Wt Percent) of MnE21 Alloy

Mn	Ce	Al	Si	Cu	Fe	Ni	Zn	Cl	Mg
1.6–2.0	0.6–1.0	≤0.015	≤0.01	≤0.008	≤0.005	≤0.001	≤0.015	≤0.002	bal

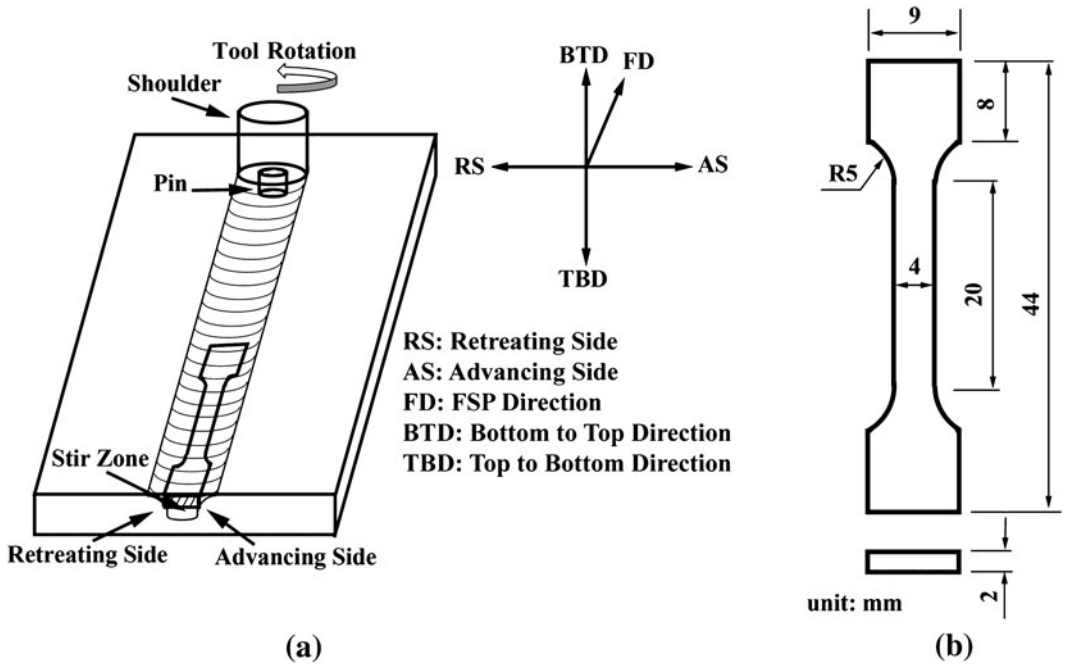

Fig. 1—Schematic illustration of (*a*) the location of tensile specimens in stir zone, and (*b*) configuration and size of tensile specimens.

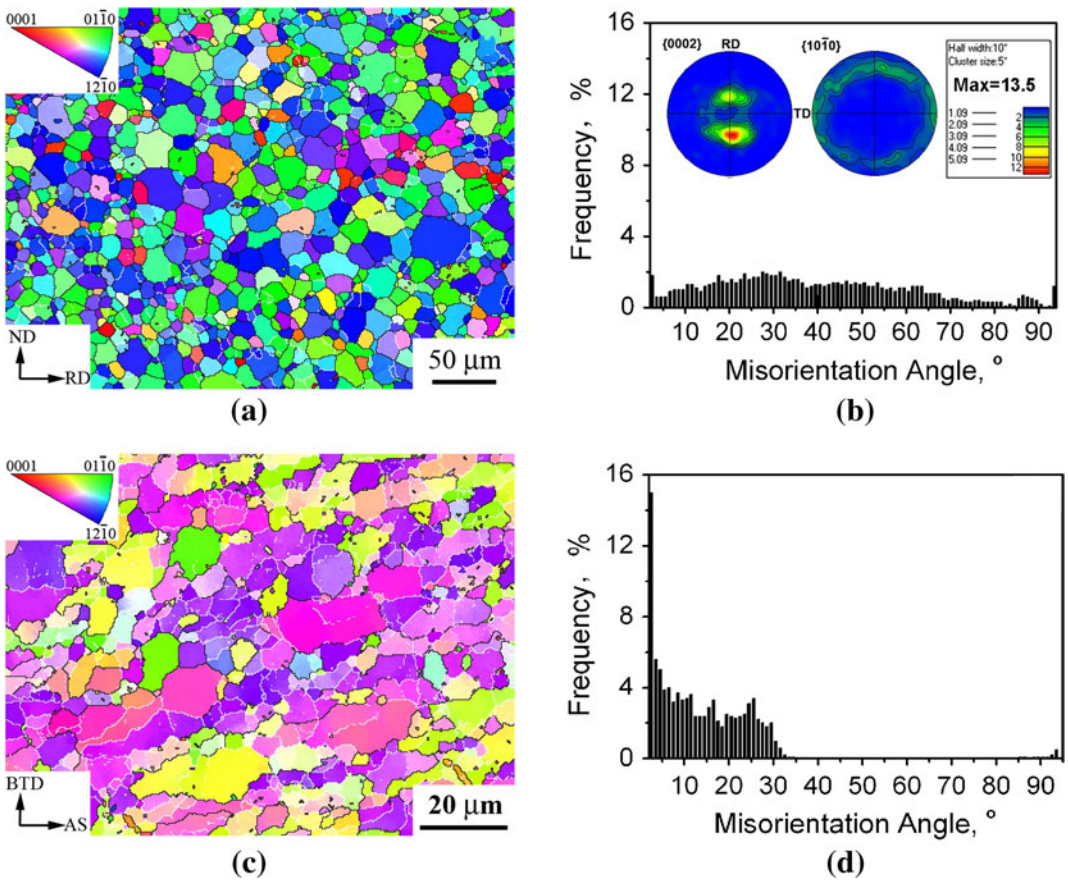

Fig. 2—EBSD results of (*a*) orientation map of HR specimen (*RD* rolling direction; *TD* transverse direction); (*b*) grain boundary misorientation angle distribution and pole figures of HR specimen; (*c*) orientation map of FSP specimen (*BTD* bottom to top direction; *AS* advancing side); (*d*) grain boundary misorientation angle distribution of FSP specimen.

of the grains were elongated and tended to align with the pin rotation trace and were mainly separated by LAGBs. A few fine equiaxed grains were observed along the grain boundaries, particularly at triple junctions. These fine equiaxed grains were completely surrounded by HAGBs, and contained almost no subboundaries. The misorientation distribution (Figure 2(d)) showed a sharp peak in the range from 2 to 3 deg, a broad concentration in the angular range from 2 to 30 deg, a wide gap in the misorientation interval in the range from 32 to 86 deg and a small concentration in the range from 86 to 94 deg.

Figure 3 shows the XRD patterns of the HR and FSP specimens. After FSP, there were no considerable changes in the number and the intensity of diffraction peaks, indicating that FSP did not result in significant phase solution and/or the formation of new phase in the MnE21. The diffraction peaks of Mg and Mn phases were detected in both the HR and FSP specimens. Figure 4 shows the distribution of second phases in the HR and FSP specimens. In the HR specimen (Figure 4(a)), many large Mn particles were observed. In the FSP specimen (Figure 4(b)), the size of the Mn particles was significantly reduced because of the breaking effect of the threaded pin during FSP.

B. *Tensile Properties of HR and FSP Specimens*

Figure 5(a) shows the stress–strain curves of the RD, TD, and FSP specimens. The TD specimen showed the highest flow stress and the lowest elongation. The FSP specimen exhibited the lowest flow stress and the highest elongation. The ultimate tensile strength (UTS), yield strength (YS), and elongation are plotted in Figure 5(b). The YS, UTS, and elongation of the TD specimen were 136, 238 MPa, and 19 pct, respectively. The RD specimen showed lower YS and UTS of 116 and 201 MPa, respectively, but higher elongation of 28 pct. The FSP specimen exhibited the lowest YS and UTS of 41 and 115 MPa, respectively, and the highest elongation of 64 pct. The true stress–strain curves showed that the highest true stress of 205 MPa was achieved in the FSP specimen (Figure 5(c)). It should be noted that at a true strain of 0.3 (engineering strain of 35 pct), the true stress reached 143 MPa, which is higher than the YS of both the TD and RD specimens. This demonstrates that the FSP Mg-Mn-Ce has the potential to exhibit high yield stress after deformation.

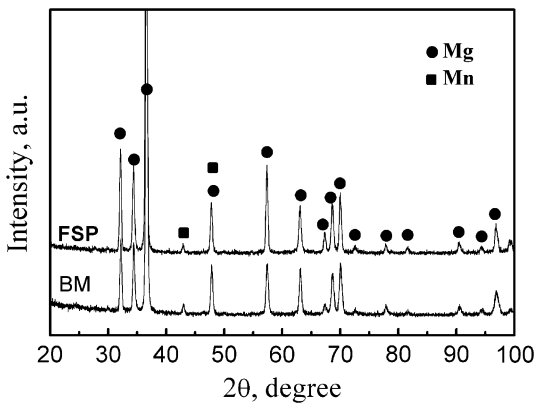

Fig. 3—XRD patterns of HR and FSP specimens.

The deformation behavior of Mg alloys at room temperature can be expressed by

$$\sigma = K\varepsilon^n \qquad [4]$$

where σ and ε are the true stress and the true strain, respectively; K is the strength coefficient; and n is the strain hardening exponent. Therefore, the value of n can be calculated by

$$n = \frac{\partial(\log\sigma)}{\partial(\log\varepsilon)} = \frac{\varepsilon}{\partial}\left(\frac{\partial\sigma}{\partial\varepsilon}\right) \qquad [5]$$

The variations of strain hardening exponent with true strain for the TD, RD, and FSP specimens are summarized in Figure 5(d). All the specimens exhibited similar n values of around 0.23 at a low strain of 0.05. The n values of all the specimens increased with the increasing strain initially. After reaching a maximum value, the n values decreased continuously with increasing the strain further. Compared with the TD specimen, the RD specimen showed higher n value increasing trend during early stage and higher n value at each strain. It is noted that the n values of the FSP specimen increased sharply to 0.82 when the strain was increased to 0.25 and then decreased continuously to 0.45 when the strain reached 0.45.

Normal anisotropy ratio (r) of the tensile specimens is summarized in Table II. The TD specimen showed the highest r value while the FSP specimen showed the lowest r value. This interesting phenomenon is because the FSP specimens were warped during the tensile test (Figure 6).

C. *Microstructural Characteristics of HR and FSP Specimens at Various Strains*

Figure 7 shows the {0002} and $\{10\bar{1}0\}$ pole figures obtained from the gages of the failed TD and RD specimens. The tensile deformation along the TD reduced the spread of the {0002} peak intensity in the TD and rotated the $\langle 10\bar{1}0\rangle$ axis roughly along the TD (Figure 7(a)). Tensile deformation along the RD reduced the basal plane tilt angles from 28 to 24 deg. The $\langle 10\bar{1}0\rangle$ axis was also roughly aligned parallel to the TD (Figure 7(b)).

Figures 8 and 9 show the {0002} and $\{10\bar{1}0\}$ pole figures obtained from various regions on the surface of the failed FSP specimens. It should be pointed out that the top and bottom surfaces of tensile specimen are 0.5 and 2.5 mm away from the FSP surface, respectively. Three observations can be made: (i) each {0002} pole figure in the gage regions showed a concentrated strong peak intensity and a dispersive weak one. The {0002} planes expressed by the strong peak intensity tended to randomly rotate around its $\langle 0002\rangle$ axis as indicated by the continuous intensity distribution of the $\{10\bar{1}0\}$. (ii) The basal plane tilt angles for grains expressed by the strong peak intensity are similar to each other in the same depth, the initial angles are ~56 deg and ~33 deg

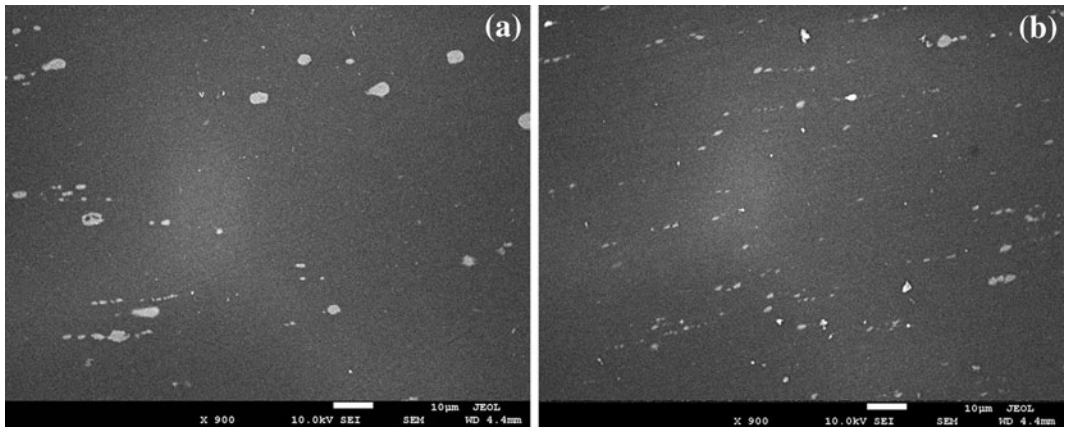

Fig. 4—Backscattered electron images of (*a*) HR and (*b*) FSP specimens.

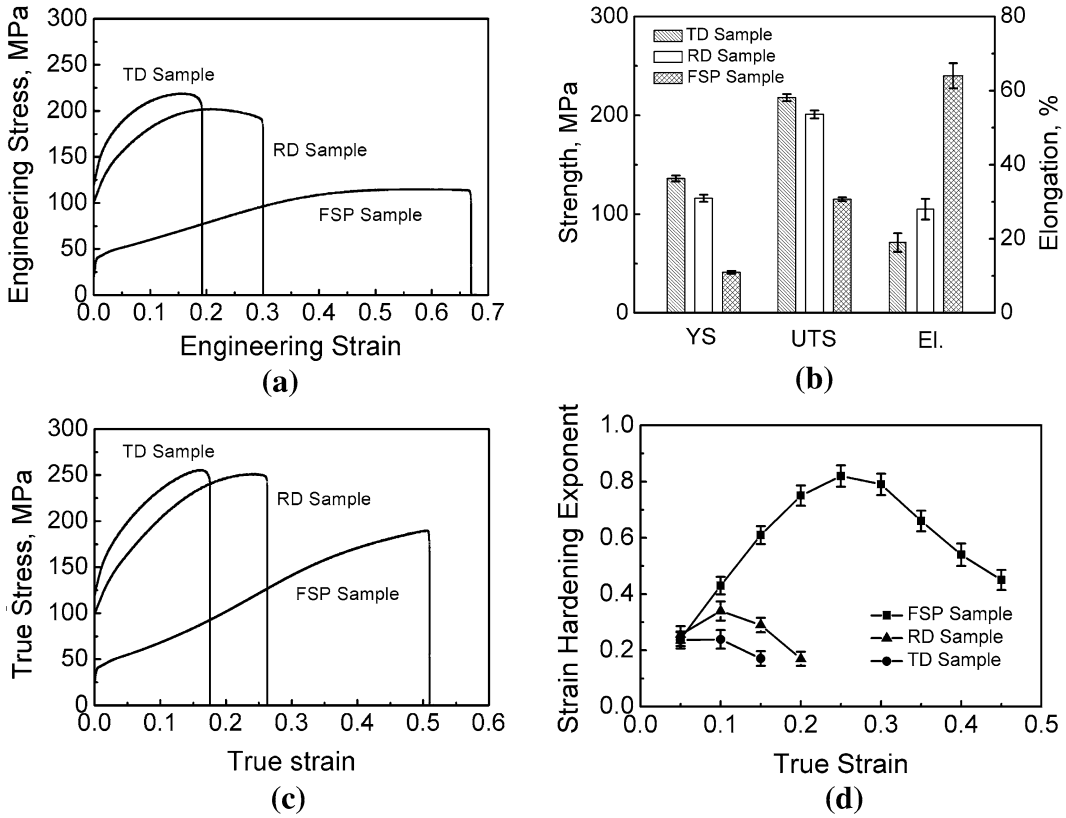

Fig. 5—Tensile properties of TD, RD, and FSP specimens: (*a*) engineering stress–strain curves, (*b*) summary of the YS, UTS, and elongation, (*c*) true stress–strain curves, and (*d*) variation of strain hardening exponent with true strain.

Table II. True Plastic Strains Along the Specimen's Width *w* (Φ_w) and Thickness *t* (Φ_t), and Normal Anisotropy Ratio (*r*) of Tensile Specimens

Specimen	Φ_w	Φ_t	*r*
TD	−0.109	−0.046	2.36
RD	−0.099	−0.117	0.85
FSP	−0.043	−0.388	0.11

on the top and bottom surfaces, respectively, but after the specimen was pulled to rupture, the angles decreased to ~27 deg and ~23 deg, respectively. (iii) The intensity of the weak peak intensity in {0002} pole figures was greatly reduced after tensile deformation in any observed region.

Based on the observations above, the microstructures at different parts of the gage developed in a similar way. Therefore, the region in the center of the bottom surface

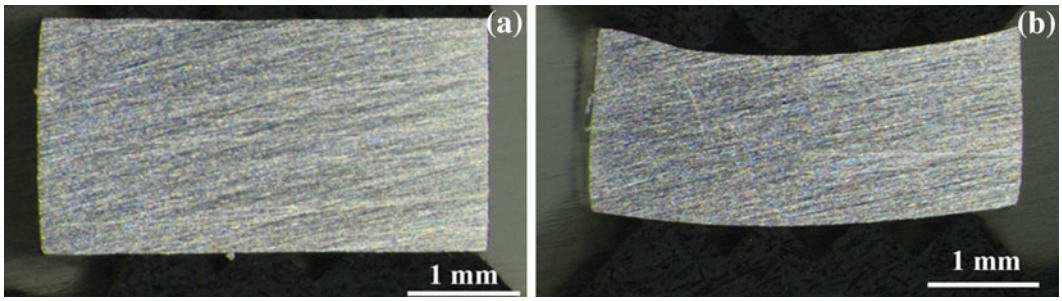

Fig. 6—Optical micrographs of the cross sections perpendicular to the tensile direction obtained from the gage regions of (*a*) undeformed, and (*b*) failed FSP specimens.

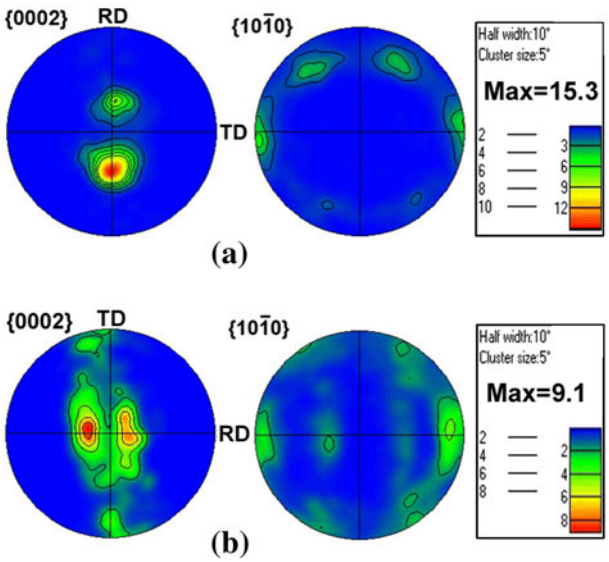

Fig. 7—Pole figures obtained from the failed (*a*) TD and (*b*) RD specimens.

was subjected to EBSD analysis at various strains (Figure 10). The microstructural characteristics observed on the bottom surface of the FSP specimen (Figure 10(a)) were mostly similar to that of cross section (Figure 2(c)), except for the appearance of banded regions which contained high density of irregular "green" grains. The "green" grains were surrounded by HAGBs in the range from 80 to 90 deg. Correspondingly, a distinct peak in the range from 80 to 90 deg was observed in the misorientation distribution (Figure 10(b)). Five EBSD maps were examined, and all of them showed the similar characteristics demonstrating that the appearance of banded regions is a common characteristic in the FSP specimen. These banded regions disappeared even at a low strain of 0.17 (Figure 10(c)).

Three microstructural evolution characteristics were observed with the strain. Firstly, the density of LAGBs in EBSD maps and the height of low-angle peak increased gradually when increasing the true strain from 0 to 0.34 (Figures 10(b), (d), and (f)) but increased sharply with further increase the true strain to 0.51 (Figures 10(f) and (h)). Secondly, newly twinned "green" grains were observed in EBSD maps at various strains (Figures 10(c), (e), and (g)). Most of the "green" grains have lost their original morphologies, and were transformed into irregular-shaped grains under the subsequent deformation. This drastically decreased the amounts of twin boundaries and scattered peak in the range from 80 to 90 deg to that from 55 to 90 deg concentration in the misorientation distribution (Figures 10(b) and (h)). Thirdly, the angles between the $\langle 0002 \rangle$ axis and tensile direction in both the matrix region and twined region increased with the increasing strain (Figures 10(b), (d), (f), and (h)).

IV. DISCUSSION

A. *Microstructural Evolution During FSP*

1. *Basal plane textural pattern*

Many studies[26–29] have tried to understand the material flow during FSW/FSP. From these results, it was deduced that the material flow mainly occurred in the tool rotating direction because of a shear stress on the surface of the FSP pin. The slip deformation of hcp Mg preferentially occurs on the {0002} basal plane. Therefore, the material flow during FSP has an influence on the distribution of the basal planes. The typical observation which was carried out by Park *et al.*[26] showed that the {0002} basal planes were roughly parallel to the pin surface in most parts of the SZ except for the regions near the upper surface. However, different textural characteristics were observed in the current study.

Figure 11 schematically shows the crystallographic orientation of Mg crystals based on the pole figures (Figures 2(d), 8 and 9). The {0002} basal planes roughly surrounded the pin from the retreating side to the advancing side (Figure 11(a)), which is similar to previous reports.[26] However, there was a large angle between the base planes and the pin surface and the angles tended to increase with increasing the depth (Figure 11(b)). This is mainly associated with the fact that the small-sized tool and low rotation rate used in the current study resulted in lower thermal input and lower material flow during FSP,[30,31] which could be further confirmed by the existence of large-sized Mn particles (Figure 4(b)) and high fraction of LAGBs (Figures 2(d) and 10(b)) in the SZ. Furthermore, the angles between the base planes and the pin surface

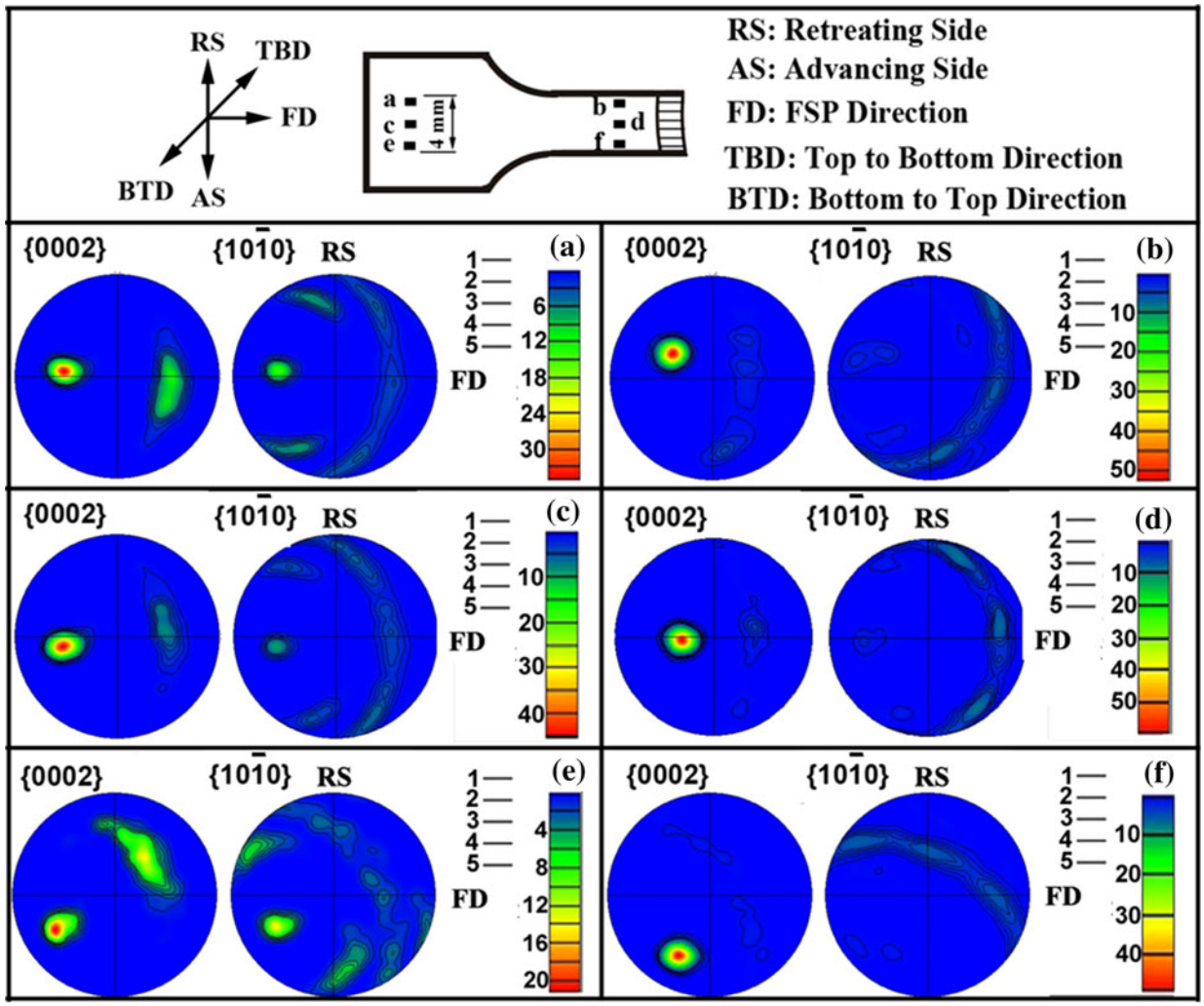

Fig. 8—Pole figures obtained from the top surface of the failed FSP tensile specimens.

tended to increase with the increasing depth. This could be attributed to the decreased deformation temperature at deep region during FSP. Therefore, a new basal plane distribution is shown in the current study (Figure 11).

2. *Grain structural evolution*

As mentioned in the previous section, the material in the SZ experienced an intense plastic deformation during FSP, producing substantial microstructural alterations, such as the crystallographic textural and grain structural evolutions.[20,26] In previous studies, FSP could produce the fine equiaxed and fully recrystallized grains with average grain sizes less than 3 μm in Al alloys[32,33] and Mg alloys.[31] However, in the current study, the SZ consisted of grains with an average size of 9 μm. This could be associated with the low material flow and special recrystallization mechanism in MnE21 alloy because of a small-sized tool and a low rotation rate.

EBSD maps (Figures 2(c) and 10(a)) showed that the microstructure can hardly be described adequately in conventional terms of just grains. Instead, the dominant microstructural feature is a mixture of HAGBs and LAGBs. This is different from the residual microstructure in the other FSP Mg alloys that exhibited an equiaxed grain structure with a high fraction of HAGBs, which is commonly referred as being "recrystallized,"[20,31,34] but is similar to the microstructure developed near the pin keyhole in FSW AZ31 Mg[35] and to the microstructure in the severely deformed materials,[36,37] in which the dislocations piled up to form LAGBs.

The FSP specimen had a strong {0002} ⟨*uvtw*⟩ B-fiber texture. This means that the grains were arbitrarily rotated around the ⟨0002⟩ axis. Owing to the limitations imposed by the symmetry of the hcp crystal structure, the maximal rotation angle around the ⟨0002⟩ axis is limited to 30 deg, since rotations to a greater angle have a symmetric equivalent with a rotation angle of less than 30 deg.[35] Therefore, the strong {0002} ⟨*uvtw*⟩ B-fiber texture resulted in a concentration from 2 to 30 deg angle range in the misorientation distribution of the FSP specimen (Figures 2(d) and 10(b)).

If the LAGB formation is dominated by the HAGB-to-LAGB transformation because of the formation of B-fiber texture, then a random misorientation distribution

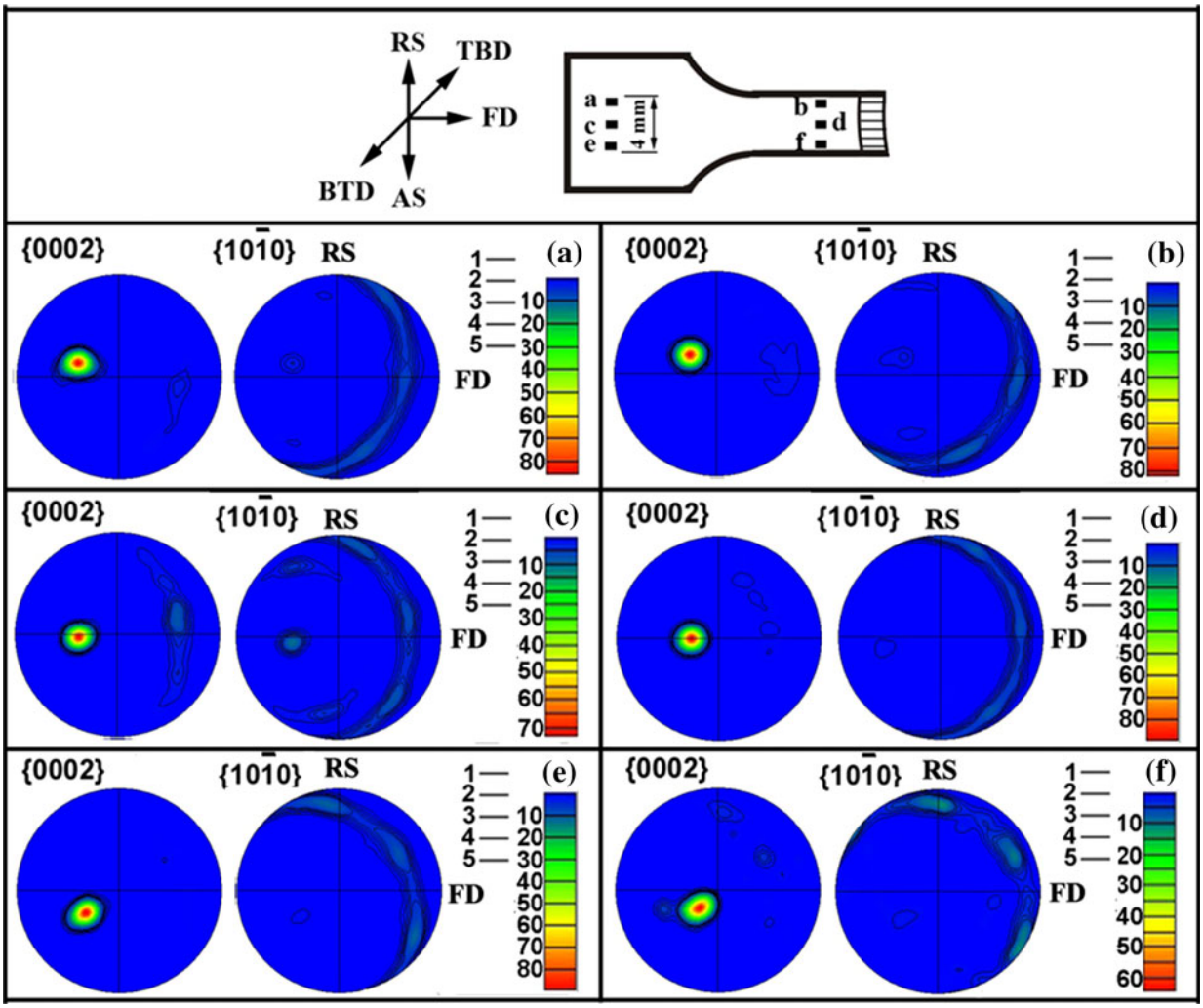

Fig. 9—Pole figures obtained from the bottom surface (2 mm below the top surface) of the failed FSP tensile specimens.

in the range from 2 to 30 deg will appear. However, a sharp peak within the range from 2 to 3 deg (Figures 2(d) and 10(b)) was observed, which should be associated with the progress that the dislocations were arranged in the form of cell walls or LAGBs during FSP. Usually, such microstructures would develop into boundaries with higher misorientations with the increasing deformation strain because of continuous absorption of dislocations on LAGBs. This mechanism of grain formation is that of continuous dynamic recrystallization (CDRX).[35–37] The recrystallized grains in the SZ being largely surrounded by the LAGBs indicate a high contribution of the CDRX during the FSP.

Further analysis showed that the crystallographic orientations of the fine grains which appeared along the grain boundaries or at the triple junctions in the SZ (Figures 2(c) and 10(a)) were not random but close to the matrix. The misorientations between the fine grains and the matrix were mostly in the range of 15 to 30 deg. This indicates that their origins are associated with the discontinuous dynamic recrystallization (DDRX).[36] The manner in which the recrystallization texture developed from a particular deformation texture and microstructure has been the subject of controversy for more than 6 decades[36], and during the whole of that period, two major theories, *i.e.*, oriented nucleation theory and oriented growth theory, have been strongly advocated. Though there is no evidence that nuclei random orientations ever occur, it still cannot confirm the origin of recrystallization texture in the current study, because the fine grains in the SZ were several microns in size, which reached the early stage of grain growth.

EBSD maps showed that the wedge- and irregular-shaped "green" grains were mainly distributed in some banded regions in the SZ (Figure 10(a)), indicating the nonuniform deformation during FSP. The misorientations between the "green" grains and the matrix are typically close to 86 deg $\langle 1\bar{2}10\rangle$, thus indicating that the active twin family is $\{10\bar{1}2\}$ extension twins.[38] The transformation of the wedge-shaped twins into irregular grains has been widely observed in Mg alloys.[39,40] During the transformation, the misorientation between the twin boundaries starts to deviate from the exact twin/matrix relationships. The above observations demonstrate that, a low proportion of $\{10\bar{1}2\}$ twins were

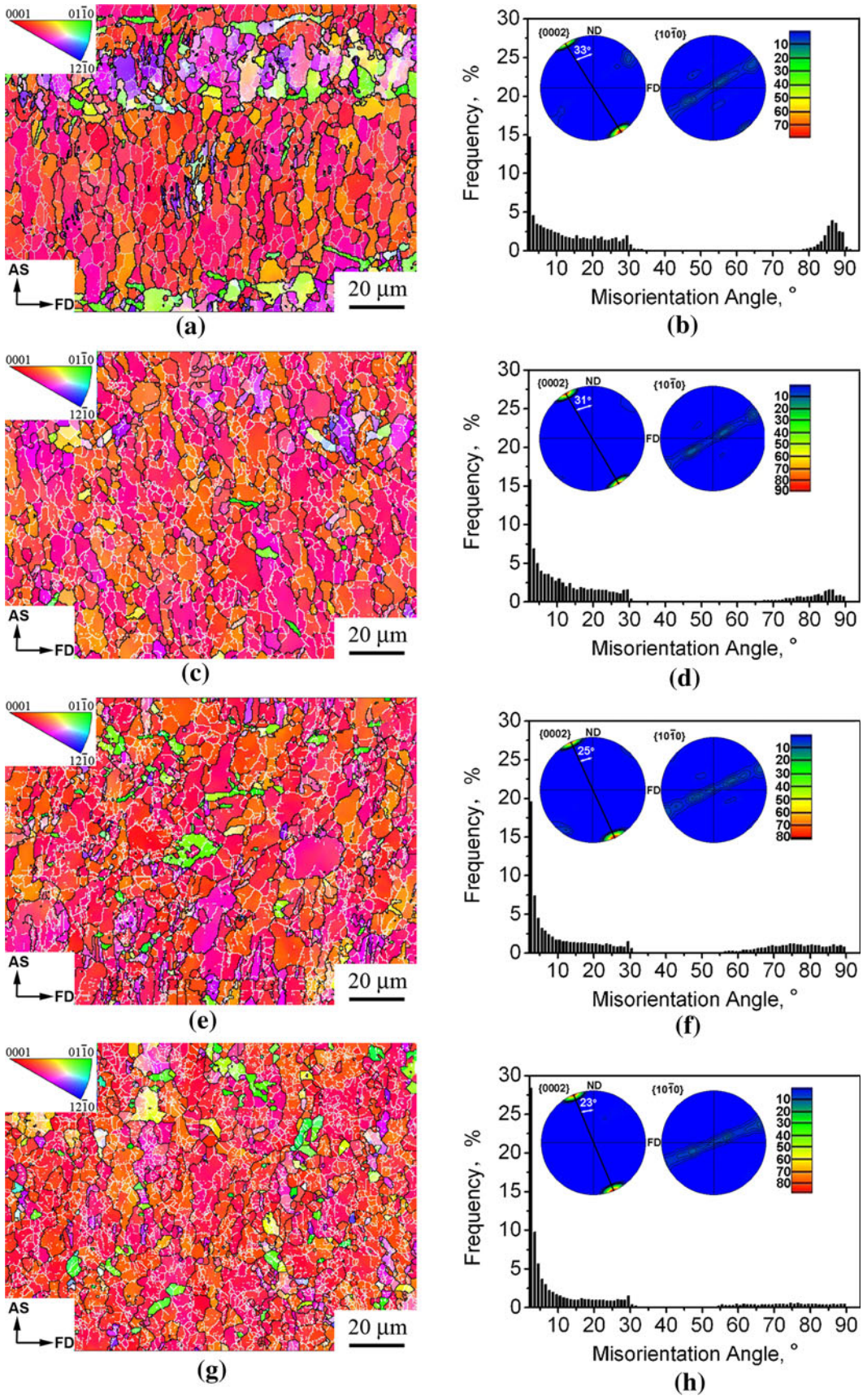

Fig. 10—EBSD results obtained from the bottom surfaces of FSP tensile specimens that deformed to true strains of (*a*), (*b*) 0; (*c*), (*d*) 0.17; (*e*), (*f*) 0.34; (*g*), (*f*) 0.51.

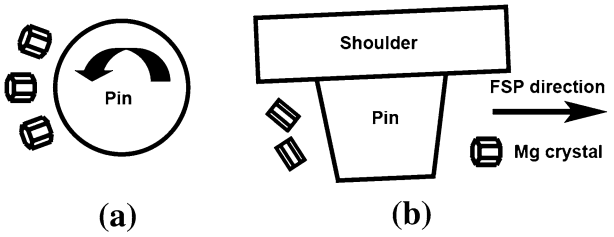

Fig. 11—Schematic illustrations showing the crystallographic orientation of Mg crystals (*a*) parallel to the FSP surface, and (*b*) along the centerline of the FSP region.

formed in the initial stage, which were then effectively destroyed by the subsequent deformation during FSP, inducing the transformation of the 86 deg twin boundaries into HAGBs in the range from ~80 to 90 deg (Figure 10(b)). This mechanism of the grain formation is that of twining dynamic recrystallization (TDRX).[20]

The microstructure of the FSP sample was characterized by extremely high density of LAGBs (Figures 2(a), (b), and 10(a), (b)). This indirectly indicates that the dynamic recrystallization of the FSP sample was not completed because of lower thermal input, slower deformation rate, and insufficient deformation strain. Such a microstructure is helpful to enable us understand the microstructural evolution of Mg alloys during FSP.

B. *Influence of Microstructural Evolution on Subsequent Tensile Deformation Behaviors*

1. *Influence of microstructural evolution on tensile elongation improvement*

In Mg-Mn-Ce alloys, higher elongations correspond well with higher *n* values (Figure 5) which represent the strong ability of the material to retard necking. When the *n* values are lower than the true strains, the Mg alloys cannot delay necking (Figure 5(d)). This is in good agreement with the well-known Consideré criterion which predicts instability as shown in References 41, 42

$$\frac{n}{\varepsilon} = \frac{1}{\partial}\left(\frac{\partial\sigma}{\partial\varepsilon}\right) \leq 1 \qquad [6]$$

The above results demonstrate that the high strain of the FSP sample was attributed to its high *n* values at various strains.

In single-crystal Mg, the CRSS for nonbasal slip is about one hundred times as large as that for basal slip.[9,10] Therefore, the basal slip is the dominant deformation mechanism at room temperature. However, in polycrystalline Mg, if only the basal slip occurs, because of the constraint by neighboring grains, then only two independent slip systems are available out of the required five. This causes strain incompatibility at the grain boundaries and gives rise to the activation of nonbasal dislocations as well as twins.[43,44] Previous studies[13,45,46] showed that the CRSS for ⟨a⟩ prismatic system is only 2 to 5 times higher than that for basal slip in polycrystalline Mg based on experiments and simulations. These results indicate that the compatibility

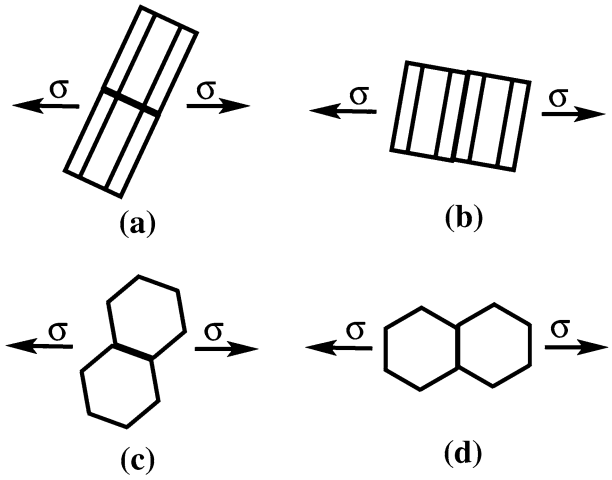

Fig. 12—Schematic illustrations showing the rearrangements of Mg crystals under the effect of (*a*); (*b*) ⟨a⟩ basal slip; and (*c*), (*d*) ⟨a⟩ prismatic slip.

effects at grain boundaries restrict the activity of basal slip and, concomitantly, enhance the activity of nonbasal slip in polycrystalline Mg.

A few reports[46,47] also showed the activation of pyramidal ⟨c + a⟩ slip at room temperature besides the basal and prismatic slips. However, in the case of tensile deformation at room temperature, the relative activity of the ⟨c + a⟩ slip to the ⟨a⟩ basal slip is less than 0.1.[46,47] This indicates that the activation of ⟨c + a⟩ is possible, but its contribution to the strain is not significant. Therefore, only basal and prismatic slips were mainly considered in the current study.

Under a uniaxial tensile deformation condition, the crystallographic orientation of each grain rotates such that the slip direction of the particular slip system with the largest Schmid factors is tilted toward the tensile axis.[44] Based on this theory, the effect of ⟨a⟩ basal slip and ⟨a⟩ prismatic slip on the distribution of Mg crystal during uniaxial tensile deformation are schematically shown in Figure 12. The crystal lattices are assumed as rigid units. The activation of basal slip (Figure 12(a)) gradually leads to the rotation of the crystal lattice to the orientation where the basal plane is aligned parallel to the tensile direction, and therefore forming a fiber texture. Simultaneously, a compressive deformation roughly along the ⟨0002⟩ axis and an extended deformation along tensile direction occur. Comparatively, the activation of prismatic slip (Figure 12(b)) gradually leads to the rotation of the crystal lattice to the orientation where the $\langle 10\bar{1}0\rangle$ axis is aligned parallel to the tensile direction. The prismatic slip also resulted in an extended deformation along the tensile direction and a compressive deformation along the direction perpendicular to both the tensile direction and ⟨0002⟩ axis. Based on the discussion above, the activation of basal and nonbasal slips can be easily recognized in the pole figures and *r* values of the tensile specimens.

High *r* value (Table II) and the phenomenon that $\langle 10\bar{1}0\rangle$ axis was aligned parallel to the tensile direction in the failed TD specimen (Figure 7(a)) demonstrated a

high contribution of prismatic slip during tensile deformation. The concentration of basal pole along the tensile direction (Figure 7(a)) indicated the occurrence of basal slip in the TD specimen which can be attributed to the fact that the Schmid factors for the basal slip in most grains are not absolutely zero. Most grains had higher Schmid factors for basal slip in the RD specimen than in the TD specimen (Figure 2(b)). Therefore, a lower applied stress was needed for the basal slip activation, resulting in lower YS in the RD specimen (Figure 5). Compared with the TD specimen, the RD specimen showed a reduced *r* value (Table II). All these indicate that the contribution of basal slip in the RD specimen was higher than that in the TD specimen. Accordingly, the contribution of prismatic slip was reduced in the RD specimen, which is further verified by its $\{10\bar{1}0\}$ pole figure (Figure 7(b)) and low flow stress (Figure 5).

The microstructural evolution during tensile deformation is complex in the FSP specimen. The concentrated strong peak and dispersive weak peak represented the basal planes of the matrix grains and TDRX grains (Figure 10), respectively, based on EBSD observations (Figures 8 through 10). Most of the matrix grains had high Schmid factor for $\langle a \rangle$ basal slip initially. Therefore, the basal slip could be activated at very low applied stresses. Upon increasing the strain from 0 to 0.17 (Figures 10(b) and (d)), the tilt angles of basal plane in the matrix grains decreased from 33 deg to 31 deg because of the basal slip. Correspondingly, the fraction of LAGBs increased with the increasing strain. Upon increasing the strain from 0.17 to 0.34 (Figures 10(d) and (f)), a great tilt angle degression from 31 deg to 25 deg was observed, indicating the extensive activation of basal slip. However, the extensive activation of basal slip did not result in a great development of subgrain boundaries (Figures 10(a), (c), and (e)). This indicates that the dominant deformation mechanism was still one of dislocation interaction and multiplication. Therefore, the maximum *n* value was observed in this stage. Upon further increasing the strain to 0.51 (Figures 10(f) and (h)), it was observed that only a small tilt angle decrease from 25 deg to 23 deg, demonstrating the reduced activation of basal slip. Simultaneously, the fraction of LAGBs increased sharply at this stage (Figures 10(e) and (g)), suggesting the high contribution of dynamic recovery. Therefore, the *n* values decreased with increasing strain in this stage. Although the distribution of prismatic planes $\{10\bar{1}0\}$ tended to be more concentrated in the failed specimens, its maximum density was still low (Figures 8 and 9). This demonstrated that the dominant deformation mechanism during the tensile deformation for the FSP specimen was one of basal slip, which was accompanied by prismatic slip.

In the current study, the gradually formed twins during tensile test rapidly lost their original shapes through boundary migration, demonstrating the occurrence of TDRX. This phenomenon is significantly different from that in twinning-induced plasticity (TWIP) steels. In the TWIP steels, the gradual formation of deformation twins during deformation increased the strain hardening because of the increased boundary density and therefore dramatically enhanced their ductility.[48,49] During TDRX, the twin boundaries migrate into highly defective region and leave perfect crystals behind them.[36] This process reduces the dislocation density. Based on the fact that only low densities of twins were observed in the FSP specimen, the contribution of $\{10\bar{1}2\}$ twin to *n* value was quit limited.

The discussion above demonstrates that the main deformation behavior of FSP Mg alloy during tensile testing should be as follows: During the initial stage of deformation, there is an increase in the flow stress and the *n* value as dislocations multiply and interact. In the meantime, the decrease of the Schmid factor for basal slip further accelerates the flow stress increment. However, as the dislocation density rises, the rate of recovery increases. A microstructure with LAGBs developed because of the rearrangement of dislocations. At a certain strain, the *n* value begins to decrease with the increasing strain because of high recovery. The specimens cannot delay rupture when the *n* value is lower than that of the true strain.

2. *Influence of textural evolution on warping phenomenon*

In order to investigate the effect of textural evolution on warping phenomenon, the {0002} pole figures are summarized on the cross section of the undeformed and the failed FSP tensile specimens (Figures 13 and 14). The peak intensities in all the pole figures tended to move away from the center toward the circumference with progress of tensile deformation. These can be attributed to the fact that the activation of basal slip gradually leads to the rotation of the basal plane to be aligned parallel to the tensile direction. When the basal slip is the dominant deformation mechanism, compressive deformation mainly occurred along the $\langle 0002 \rangle$axis. Based on the discussion above, Figure 15 schematically shows the material deformation on the cross section of the FSP specimen under the action of basal slip. There are large deformation components along the thickness and low deformation components along the width. This model corresponds well with the fact that deformation mainly occurred along the thickness. At both sides of the upper parts, the deformation components along the width move the material toward the centerline. Conversely, at both sides of the lower parts, the deformation components along the width move material outward from the centerline. Under the action of the opposite deformation components, the tensile specimens warped in the entire gage parts. This further confirms that the tensile deformation of the FSP specimen was mainly controlled by the basal slip.

C. *Deformation Ability and Flow Stress*

The current FSP Mg-Mn-Ce alloy possesses a large portion of grains in orientations with many {0002} planes aligning nearly 45 deg with respect to the FSP direction, and therefore exhibits low initial flow stress, enhanced *n* values, and excellent deformation ability when tensile stress was applied along the FSP direction.

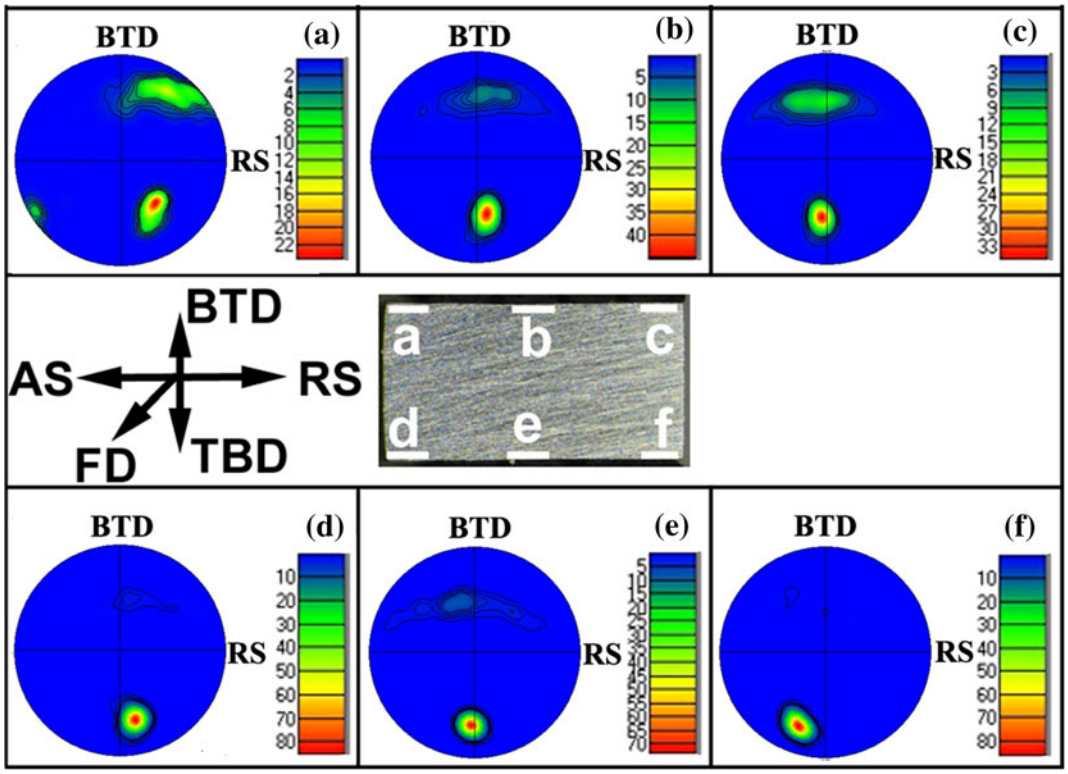

Fig. 13—{0002} pole figures summarized on cross section of undeformed FSP tensile specimen.

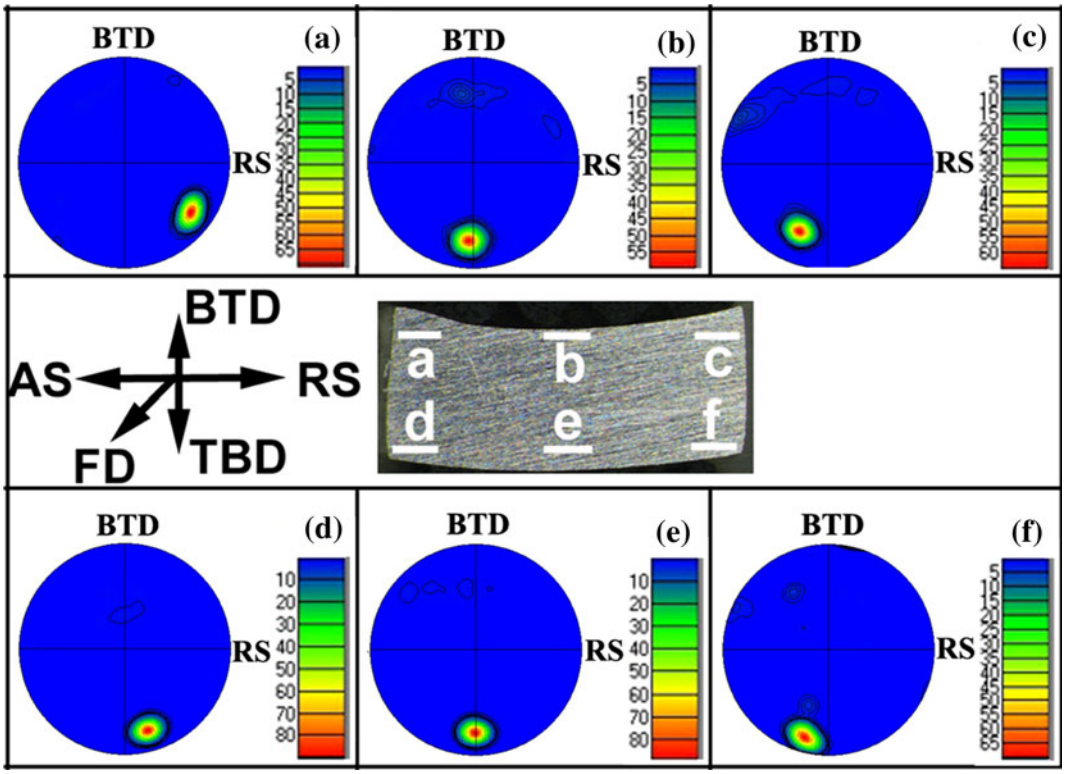

Fig. 14—{0002} pole figures summarized on cross section of the failed FSP tensile specimen.

This result provides a potential solution to enhance the deformation ability of Mg alloys by textural reconstruction.

The significant gain of the tensile strain in magnesium alloys through textural reconstruction is inevitably sacrificed by the loss of the YS. The inadequate YS

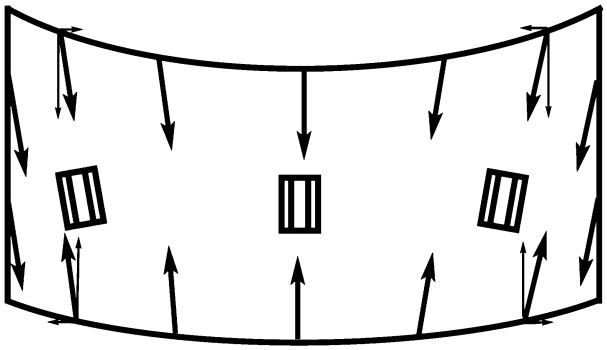

Fig. 15—Schematic illustration showing the material deformation on the cross section of FSP tensile specimen under the action of basal slip.

would be a hurdle if using the FSP Mg alloys as load-bearing materials without any additional treatments. The authors believed that the YS of the alloys can be enhanced through alloying, grain refinement, or other solutions. These are the challenges that we shall deal with in the future. From another perspective, the lower flow stress satisfies the forming requirement because it is beneficial for reducing the power required of the forming equipment and prolonging the die life.

V. CONCLUSIONS

1. FSP produced fine grains 9 μm in size in a HR Mg-Mn-Ce alloy. Most of the grains were elongated along the pin rotation trace and were mainly separated by LAGBs. A few fine equiaxed grains and wedge-shaped twins were also observed.
2. A new basal plane texture was developed in the SZ because of the low thermal input and material flow during FSP. The {0002} basal planes roughly surrounded the pin from the retreating side to the advancing side. However, there was a large angle between the base planes and the pin surface and the angles tended to increase with increasing the depth.
3. EBSD analysis showed that the recrystallization mechanism during FSP is mainly CDRX, but also associated with DDRX and TDRX.
4. An enhanced ⟨a⟩ basal slip during tensile deformation in FSP specimen resulted in significantly increased n values, a high ductility and a reduced r value. This demonstrated that facilitating basal slip in polycrystalline Mg alloys by textural reconstruction using FSP is an effective method of increasing their deformation abilities.
5. The deformation behavior of FSP Mg alloy during tensile test is as follows. The flow stress increased with strain initially because of the increase in the Schmid factors for basal slip combined with dislocation multiplication and interaction. New LAGBs were developed because of the rearrangement of dislocations. At a certain strain, the n value began to decrease with further increasing strain because of high recovery. Fracture occurred when the n value was lower than the true strain.
6. A material flow model, developed based on the local textural evolution on the cross section of FSP tensile specimen, can reasonably explain the warping phenomenon during tension.

ACKNOWLEDGMENTS

The authors gratefully acknowledge the support of (a) ASTAR SERC of Singapore under grant no. 0921370018, and (b) the National Natural Science Foundation of China under Grant no. 50890171.

REFERENCES

1. T.G. Langdon: *Mater. Trans.*, 1999, vol. 40, pp. 716–22.
2. N. Afrin, D.L. Chen, X. Cao, and M. Jahazi: *Scripta Mater.*, 2007, vol. 57, pp. 1004–07.
3. G.S. Rao and Y.V.R.K. Prasad: *Metall. Trans. A*, 1982, vol. 13A, pp. 2219–26.
4. W.J. Kim, S.W. Chung, C.S. Chung, and D. Kum: *Acta Mater.*, 2001, vol. 49, pp. 3337–45.
5. W.J. Kim, S.I. Hong, Y.S. Kim, S.H. Min, H.T. Jeong, and J.D. Lee: *Acta Mater.*, 2003, vol. 51, pp. 3293–3307.
6. Y.C. Xin, M.Y. Wang, Z. Zeng, G.J. Huang, and Q. Liu: *Scripta Mater.*, 2011, vol. 64, pp. 986–89.
7. Q. Yang and A.K. Ghosh: *Acta Mater.*, 2006, vol. 54, pp. 5159–70.
8. S.R. Agnew, J.A. Horton, T.M. Lillo, and D.W. Brown: *Scripta Mater.*, 2004, vol. 50, pp. 377–81.
9. H. Yoshinaga and R. Horiuchi: *Trans JIM*, 1963, vol. 4, pp. 1–8.
10. T. Obara, H. Yoshinaga, and S. Morozumi: *Acta Metall.*, 1973, vol. 21, pp. 845–53.
11. M.R. Barnett: *Metall. Mater. Trans. A*, 2003, vol. 34A, pp. 1799–1806.
12. J. Bohlen, M.R Nürnberg, J.W. Senn, D. Letzig, and S.R. Agnew: *Acta Mater.*, 2007, vol. 55, pp. 2101–12.
13. A. Styczynski, C. Hartig, J. Bohlen, and D. Letzig: *Scripta Mater.*, 2004, vol. 50, pp. 943–47.
14. H.L. Ding, L.F. Liu, S. Kamado, W.J. Ding, and Y. Kojima: *J. Alloy. Compd.*, 2008, vol. 456, pp. 400–06.
15. Y. Yoshida, L. Cisar, S. Kamado, and Y. Kojima: *Mater. Trans.*, 2003, vol. 44, pp. 468–75.
16. R.S. Mishra and Z.Y. Ma: *Mater. Sci. Eng. R*, 2005, vol. 50, pp. 1–78.
17. Z.Y. Ma, F.C. Liu, and R.S. Mishra: *Acta Mater.*, 2010, vol. 58, pp. 4693–4704.
18. F.C. Liu and Z.Y. Ma: *Scripta Mater.*, 2008, vol. 59, pp. 882–85.
19. A.H. Feng and Z.Y. Ma: *Scripta Mater.*, 2007, vol. 56, pp. 397–400.
20. A.H. Feng and Z.Y. Ma: *Acta Mater.*, 2009, vol. 57, pp. 4248–60.
21. W. Woo, H. Choo, M.B. Prime, Z. Feng, and B. Clausen: *Acta Mater.*, 2008, vol. 56, pp. 1701–11.
22. W. Woo, H. Choo, D.W. Brown, P.K. Liaw, and Z. Feng: *Scripta Mater.*, 2006, vol. 54, pp. 1859–64.
23. H.W. Lee, T.S. Lui, and L.H. Chen: *J. Alloy. Compd.*, 2009, vol. 475, pp. 139–44.
24. http://www.stolfig.de/services/forschung.php 2012.
25. S.R. Agnew and O. Duygulu: *Int. J. Plasticity*, 2005, vol. 21, pp. 1161–93.
26. S.H. Park, Y.S. Sato, and H. Kokawa: *Metall. Mater. Trans. A*, 2003, vol. 34A, pp. 987–93.
27. T.U. Seidel and A.P. Reynolds: *Metall. Mater. Trans. A*, 2001, vol. 32A, pp. 2879–84.
28. G.R. Cui, Z.Y. Ma, and S.X. Li: *Acta Mater.*, 2009, vol. 57, pp. 5718–29.
29. K.N. Krishnan: *Mater. Sci. Eng. A*, 2002, vol. 327, pp. 246–51.
30. F.C. Liu and Z.Y. Ma: *Metall. Mater. Trans. A*, 2008, vol. 39A, pp. 2378–88.

31. J. Chen, H. Fujii, Y.F. Sun, Y. Morisada, K. Kondoh, and K. Hashimoto: *Mater. Sci. Eng. A*, 2012, vol. 549, pp. 176–84.
32. F.C. Liu, B.L. Xiao, K. Wang, and Z.Y. Ma: *Mater. Sci. Eng. A*, 2010, vol. 527, pp. 4191–96.
33. F.C. Liu and Z.Y. Ma: *Mater. Sci. Eng. A*, 2011, vol. 530, pp. 548–58.
34. Q. Yang, B.L. Xiao, and Z.Y. Ma: *J. Alloy Compd.*, 2013, vol. 551, pp. 61–66.
35. U.F.H.R. Suhuddin, S. Mironov, Y.S. Sato, H. Kokawa, and C.W. Lee: *Acta Mater.*, 2009, vol. 57, pp. 5406–18.
36. F.J. Humphreys and M. Hatherly. *Recrystallization and Related Annealing Phenomena*. Elsevier, Amsterdam, 2004, pp. 415–24.
37. Y. Iwahashi, Z. Horita, M. Nemoto, and T.G. Langdon: *Acta Mater.*, 1997, vol. 45, pp. 4733–41.
38. M.D. Nave and M.R. Barnett: *Scripta Mater.*, 2004, vol. 51, pp. 881–85.
39. A.G. Beer and M.R. Barnett: *Metall. Mater. Trans. A*, 2007, vol. 38A, pp. 1856–67.
40. T. Al-Samman and G. Gottstein: *Mater. Sci. Eng. A*, 2008, vol. 490, pp. 411–20.
41. Y. Champion, C. Langlois, S.G. Mailly, P. Langlois, J.L. Bonnentien, and J. Hÿtch: *Science*, 2003, vol. 300, pp. 310–11.
42. D. Jia, Y.M. Wang, K.T. Ramesh, E. Ma, Y.T. Zhu, and R.Z. Valiev: *Appl. Phys. Lett.*, 2001, vol. 79, pp. 611–13.
43. C.K. Chyung and C.T. Wei: *Phil. Mag.*, 1967, vol. 15, pp. 161–75.
44. V. Jayaram: *Acta Metall.*, 1987, vol. 35, pp. 1307–15.
45. J. Koike and R. Ohyama: *Acta Mater.*, 2005, vol. 53, pp. 1963–72.
46. S.R. Agnew, C.N. Tomé, D.W. Brown, T.M. Holden, and S.C. Vogel: *Scripta Mater.*, 2003, vol. 48, pp. 1003–08.
47. S.R. Agnew, M.H. Yoo, and C.N. Tomé: *Acta Mater.*, 2001, vol. 49, pp. 4277–89.
48. F.C. Liu, Z.N. Yang, C.L. Zheng, and F.C. Zhang: *Scripta Mater.*, 2012, vol. 66, pp. 431–34.
49. O. Grassel, L. Kruger, G. Frommeter, and L.W. Meyer: *Int. J. Plast*, 2000, vol. 16, pp. 1391–1409.